FULL PAPER

# Silicon-Modified Rare-Earth Transitions—A New Route to Near- and Mid-IR Photonics

*Manon A. Lourenço,\* Mark A. Hughes, Khue T. Lai, Imran M. Sofi, Willy Ludurczak, Lewis Wong, Russell M. Gwilliam, and Kevin P. Homewood*

**Silicon underpins microelectronics but lacks the photonic capability needed for next-generation systems and currently relies on a highly undesirable hybridization of separate discrete devices using direct band gap semiconductors. Rare-earth (RE) implantation is a promising approach to bestow photonic capability to silicon but is limited to internal RE transition wavelengths. Reported here is the first observation of direct optical transitions from the silicon band edge to internal *f*-levels of implanted REs (Ce, Eu, and Yb); this overturns previously held assumptions about the alignment of RE levels to the silicon band gap. The photoluminescence lines are massively redshifted to several technologically useful wavelengths and modeling of their splitting indicates that they must originate from the REs. Eu-implanted silicon devices display a greatly enhanced electroluminescence efficiency of 8%. Also observed is the first crystal field splitting in Ce luminescence. Mid-IR silicon photodetectors with specific detectivities comparable to existing state-of-the-art mid-IR detectors are demonstrated.**

## 1. Introduction

Silicon underpins the whole of microelectronics and the digital world as we know it. Despite being the "champion" electronic semiconductor it lacks key photonic capability needed for next-generation systems and currently relies on separate discrete

Dr. M. A. Lourenço, Dr. M. A. Hughes, Dr. K. T. Lai,
I. M. Sofi, Dr. W. Ludurczak, Dr. L. Wong,
Prof. R. M. Gwilliam, Prof. K. P. Homewood
Advanced Technology Institute
Faculty of Engineering and Physical Sciences
University of Surrey
Guildford, Surrey GU2 7XH, UK
E-mail: m.lourenco@surrey.ac.uk
Dr M. A. Hughes
Joule Physics Laboratory
School of Computing
Science and Engineering
University of Salford
Salford M5 4WT, UK
I. M. Sofi
British Malaysian Institute
Universiti Kuala Lumpur
1016 Jalan Sultan Ismail, 50250 Kuala Lumpur, Malaysia

devices using alternative direct band gap semiconductors. This hybridization is highly undesirable, seriously violating the paramount technological and cost advantages inherent in silicon integration that has driven its exponential growth. The ultimate vision of silicon integration is a totally single silicon solution incorporating both electronic and photonic functions. Here we report a novel phenomenon—silicon-modified rare-earth (RE) transitions—and demonstrate light emitting diodes (LEDs) and mid-IR photodetectors. Universally, luminescence from RE-doped semiconductors has shown only the expected characteristic intrinsic transitions; consequently emission from REs with transitions greater than the semiconductor band gap energy should not occur. Europium, ytterbium, and cerium have their lowest energy transitions well above the band gap energy of silicon. Remarkably, we see photoluminescence (PL) and electroluminescence (EL) due to Eu, Yb, and Ce in silicon but dramatically redshifted in wavelength and strikingly enhanced in intensity by up to 900 times compared with conventional RE-doped silicon LEDs. These results refute previous thinking on the interaction of REs with semiconductors and offer a promising route to efficient, fully silicon-based, optoelectronic devices across the near- and mid-IR.

Silicon photonics has seen rapid advances[1–12] and the technology is seen not just as required for next-generation computers but also as a vehicle for a wide range of other high value and important, societal, environmental, security, and health applications, such as greenhouse gas and explosive residue sensing, and fast medical diagnostics.[13] REs elements in silicon have long been considered promising for optical sources, and more recently for quantum technologies.[14] The partially filled inner 4*f*-shell gives sharp internal transitions highly insensitive to crystal host and temperature and many of the transitions have intrinsic gain and support lasing. However, because the transitions are internal to the RE they have not been seen so far as a particularly promising route to photodetectors.

Light emission at 1.54 μm due to Er ions in III–V and Si has been extensively investigated and light emitting devices successfully demonstrated although with limited efficiency.[15–21] PL and EL from silicon and III–V semiconductors incorporating the RE thulium have also been achieved—transitions between the $Tm^{3+}$ lowest excited states and the ground state lead to emissions around 0.8, 1.2, and 2 μm.[22–24] Both Er and Tm in silicon, and indeed all others RE reported in silicon

and other standard semiconductors behave "conventionally"—emitting at their well-known characteristic internal transition wavelengths.[25–27]

Here we investigate the incorporation of the RE elements Eu, Yb, and Ce in silicon—REs that have their lowest energy internal transitions above the band gap energy of silicon (1.1 eV). The lowest energy internal transitions of the $Eu^{3+}$ are in the red at ≈2 eV, in Yb they are in the near-IR at ≈1.3 eV, and in Ce they are in the UV/blue (3–4 eV). All these transitions are at energies greater than the silicon band gap and conventional wisdom holds that emission due to these REs could not occur in silicon. Light emission in several larger band gap semiconductors and other hosts incorporating $Eu^{3+}$, $Yb^{3+}$, and $Ce^{3+}$ has been previously reported.[28–33] PL at low temperatures was the main technique used to optically characterize these materials. Luminescence due to their well-known RE internal transitions is observed at ≈615 nm for Eu, 980 nm for Yb, and in the UV/blue (300–400 nm) for Ce. For Eu, these are the lowest energy transitions from the $^5D_0$ excited state to the $^7F_J$ states ($J$ = 0–6); for Yb, PL emission is due to the $^2F_{5/2}$–$^2F_{7/2}$ internal transitions; and for Ce, these are from the lowest lying $5d^1$ level to the lowest excited $4f$ manifold ($^2F_{7/2}$) and to the ground state manifold ($^2F_{5/2}$)—both Ce bands are broad due to the unshielded starting $5d^1$ state. We report here on PL and EL from LEDs made by ion implantation of Eu, Yb, and Ce into standard silicon substrates. Remarkably, emission due to Eu, Yb, and Ce states is observed but in all these cases it has been dramatically redshifted. The shifts are from the visible to the IR ≈1.4–1.5 µm for the Eu-doped silicon, from 980 nm to ≈1.3 µm for the Yb-doped silicon, and from two bands in the UV/blue spectral regions to 1.4 and 1.9 µm IR regions for Ce. We attribute these redshifts to transitions from carriers in silicon to the $^7F_J$ states ($J$ = 0–3) for Eu; from the silicon to the $^2F_{7/2}$ ground state manifold for Yb; and from the silicon to the $^2F_{5/2}$ ground state and the $^2F_{7/2}$ manifolds for Ce, respectively. Crystal field analysis shows that the observed PL lines must originate from the implanted REs.

Previous observations have shown that universally, when luminescence is observed from REs in conventional semiconductors only the characteristic transitions between the internal levels are seen. These transitions are excited by indirect energy transfer from recombining electrons and holes. The direct interaction shown here between bulk silicon states of the host and individual intrinsic RE levels is, we believe, unique in conventional semiconductor systems. This could be highly significant for their application in semiconductor optoelectronic devices particularly, as demonstrated here, in the technologically and commercially most significant semiconductor—silicon. Significantly, the new Eu 1.4–1.5 µm, the Yb 1.3 µm, and the Ce 1.4 and 1.9 µm emissions are the wavelengths of most importance in optical communications systems.

## 2. Results

### 2.1. Silicon Band-Edge-Modified Rare-Earth Luminescence

In **Figure 1**, we show the PL measured at 20 K from (a) Eu, (b) Yb, and (c) Ce-doped silicon p–n junctions. The EL spectra measured at 80 K are shown in Figure 1d. For comparison, we

also show, in Figure 1a, the spectra for silicon control samples which were implanted with boron only and with europium only and processed under otherwise identical conditions—for the control samples only the band-edge silicon emission is observed and there is no radiative defect emission caused by the implants. This is also the case for the Yb and Ce controls (not shown). The importance of the boron in enabling the RE emission in silicon is clear. The mechanism for boron enabling and enhancing luminescence has been previously extensively reported for both bulk and RE doped silicon.[1,20,23,24,26,27] For Eu, Yb, and Ce, distinct main lines can be seen on all the spectra with additional fine structure. These spectra do not correspond to any known implant damage induced spectra in the literature[34] and not to spectra associated with the well-known silicon D-line defects[35] or, as far as we are aware, any previously reported spectra in silicon. In addition, the spectra for Eu, Yb, and Ce are quite different from each other, despite having similar atomic masses, and quite distinct from PL and EL spectra of all other RE we have previously studied[27] when all implanted at the same doses and with the same thermal processing. These include Sm and Gd, which bracket Eu, and Tm and Pr, which are adjacent to Yb and Ce, respectively, in the lanthanide series. We have also measured EL from the Eu, Yb, and Ce LEDs under conventional forward bias from 80 K to room temperature. The EL measurements show the same spectral characteristics as the PL at the corresponding measurement temperatures. The EL quenches as the temperature is raised but can still be clearly seen up to 240 K. We believe that further optimization of the annealing conditions could lead to room and high-temperature emission as observed previously in undoped silicon LEDs.[1]

The Eu, Yb, and Ce spectra are immediately suggestive of RE transitions but are unexpectedly in the wrong energy range, far too low, for the lowest allowed internal transitions which are all much greater than the silicon band gap energy. Further, the peak positions of the lines broaden and move with measurement temperature, closely following the silicon band-edge temperature dependence, unlike internal RE transitions which are temperature invariant. Note that this temperature dependence implies that the absolute energies of the silicon RE "manifolds" are temperature independent, as expected for REs. **Figure 2** shows a comparison of the PL spectrum of Eu in silicon with a Eu spectrum from a zinc oxide host.[30] The upper plot shows PL data in the 5500–8000 $cm^{-1}$ range measured at 20 K and at 80 K from silicon samples coimplanted with B and Eu (Si:B&Eu). The lower plot shows the usual $Eu^{3+}$ PL spectrum in the visible (14700–17200 $cm^{-1}$), in this case in a ZnO host abstracted from ref.[30], taken at 10 K. The energy scales for the upper and lower plots are the same but have been displaced in energy to aid direct comparison of the relative peak positions. The spectra have been matched at the $F_0$ terminal state, which required a blueshift of our data by 9200 wavenumbers (1.14 eV). The ZnO spectral features labeled in Figure 2, as in ref.[30], correspond to the usual $^5D_0$ to $^7F_J$ ($J$ = 0 to 3) multiplets observed in $Eu^{3+}$. The corresponding transitions observed in the Si:B&Eu p–n junctions are attributed to silicon transitions to the same $^7F_J$ multiplets. The close coincidence in the energy spacing of the spectral features in the two materials is striking, particularly given the different hosts, and well within the
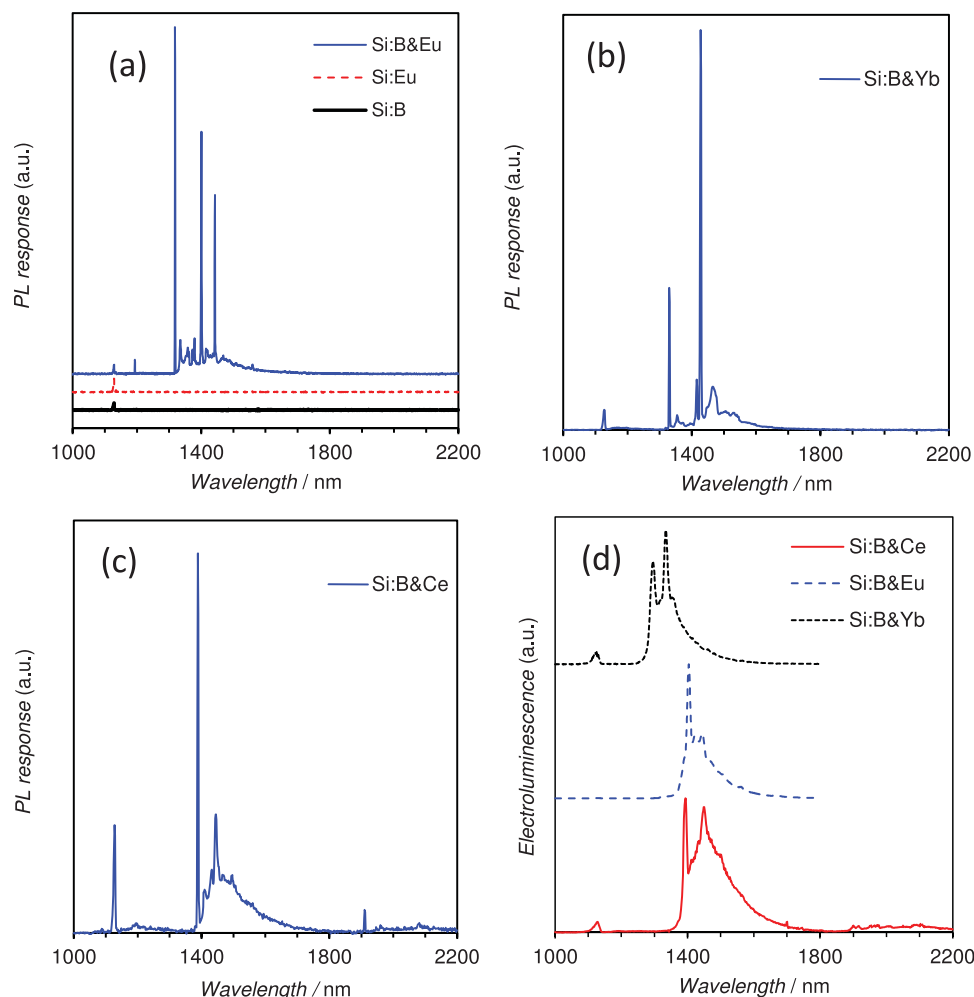
**Figure 1.** Luminescence spectra of Eu, Yb, and Ce-doped silicon p–n junctions. a) PL at 20 K of silicon coimplanted with B and Eu, of a control sample implanted with B only and of a control sample implanted with Eu only. All samples have otherwise been identically processed. The spectra have been displaced for clarity. b) PL at 20 K of silicon coimplanted with B and Yb. c) PL at 20 K of silicon coimplanted with B and Ce. d) EL at 80 K from Ce, Eu, and Yb LEDs measured at a forward bias of 1 V and a forward current density of 3.1 A cm$^{-2}$.

spread expected between different hosts. Because of totally different selection rules and hosts, we would not expect any exact correspondence of the peak intensities. The better resolved features in our Si:B&Eu spectra are attributed to the much higher crystal quality compared to the ZnO nanocrystals. Our Si:B&Eu results show a clear correspondence with the published data from many hosts, once blueshifted.

We have previously carried out a detailed crystal field analysis in silicon of two "classical" REs, i.e., REs that show only the expected internal transitions, Dy and Tm, and used a point charge model to determine that the REs sit in a substitutional, rather than an interstitial Si site.[14] Here, in addition to Eu, Yb, and Ce, a crystal field analysis of Ho was also performed for completeness. Crystal field parameters (CFPs) are structural factors which represent the symmetry of the RE's environment.[36] Local symmetry was determined by fitting sets of CFPs corresponding to commonly occurring symmetries to the experimental ground state splittings determined from PL measurements (see the Experimental Section). The results are listed in **Table 1** which shows that the best fit occurs for tetragonal

symmetry for all the REs. For cubic symmetry, the constraints $B_4^4 = 5B_0^4$ and $B_4^6 = -21B_0^6$ apply.[37]

**Figure 3**a shows a comparison of the experimental splittings from our Eu data and the fits obtained from the crystal field analysis as well as the calculated energy levels for the Eu$^{3+}$ free ions. The CFP values obtained and the spin–orbit coupling coefficients used for Ce, Eu, Yb, Dy, Ho, and Tm are listed in **Table 2** and plotted as a function of the number of $f$ electrons in Figure 3b. It can be seen that the calculated CFPs for both the classic and modified REs show a clear trend across the lanthanide series. The theoretical fits to the energy levels and the peaks selected from the experimental data for the crystal field analysis for Si:B&Yb and Si:B&Ce are shown in **Figures 4** and **5**, respectively.

If the fitted PL peaks originate from transitions to RE $f$-shells energy levels we would first expect that these peaks are reasonably close to those observed; second the same sets of CFPs (corresponding to the same symmetry) are the best fit for all the REs; and third, and most importantly, that there is a trend in the CFPs across the lanthanide series, as this would be the
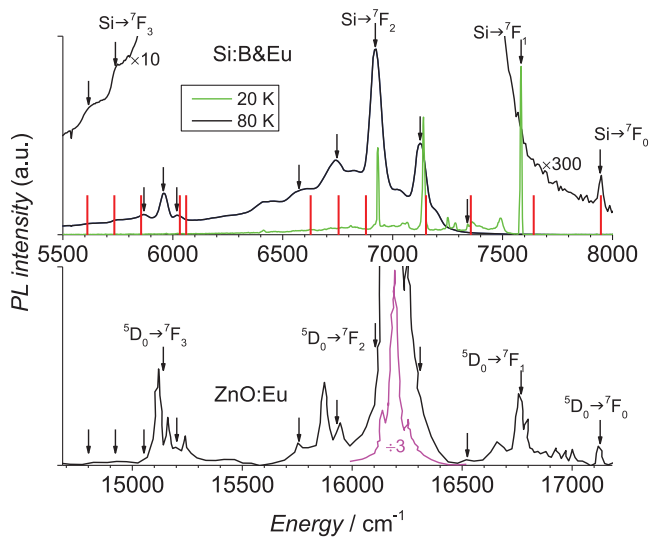
www.MaterialsViews.com

ADVANCED
FUNCTIONAL
MATERIALS
www.afm-journal.de

FULL PAPER

**Figure 2.** Comparison of the PL spectrum of Eu in Si:B&Eu with a Eu spectrum from a ZnO host.[30] The upper graph shows the PL data from a Si:B&Eu p–n junction measured at 20 K (green line) and data from a second Si:B&Eu p–n junction measured at 80 K (black line). The lower plot shows the usual $Eu^{3+}$ PL spectrum in the visible, in this case in a ZnO host taken at 10 K. The energy scales for upper and lower spectra are the same (identical energy increments) but have been displaced to aid direct comparison of the relative peak positions. Spectra have been matched to the $F_0$ terminal state. The vertical red lines on the Si:B&Eu plot are theoretical fits obtained from the crystal field analysis. The solid black arrows indicate the peaks selected from the Si:B&Eu spectra for the crystal field analysis—their corresponding energies in the displaced Zn:O spectrum are also shown.
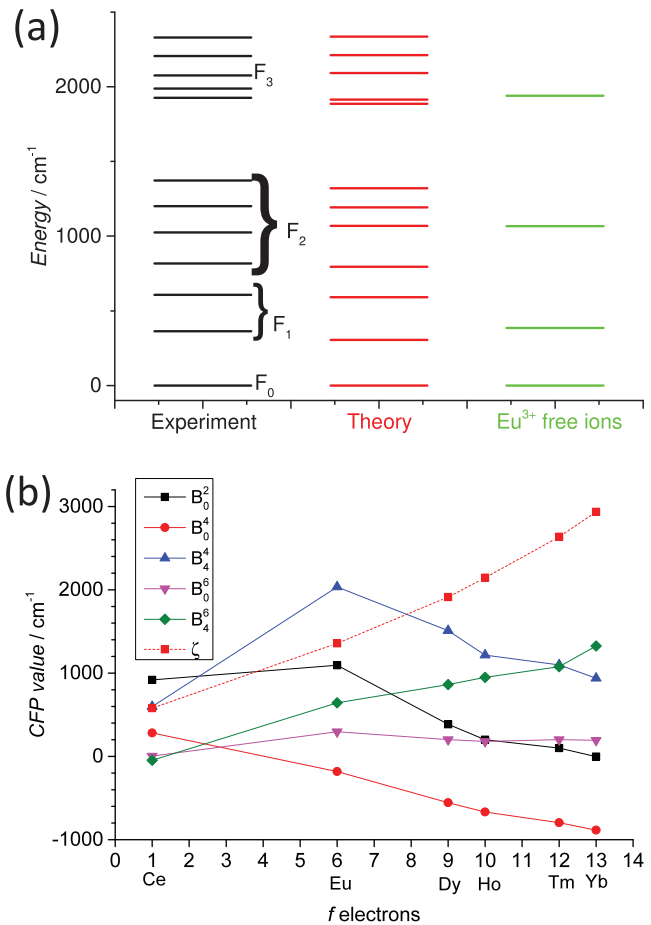


**Figure 3.** a) Comparison of experimental splittings from Si:B&Eu p–n junction data and the theoretical fits obtained from the crystal field analysis. The energy splittings in the free $Eu^{3+}$ are also shown. b) CFP values obtained and the spin–orbit coupling coefficients ($\zeta$) used for Ce, Eu, Yb, Dy, Ho, and Tm plotted as a function of the number of $f$ electrons.

most improbable observation if the peaks do not originate from REs. All of these expectations are met in our fitting, confirming that the observed PL lines that we fitted originate from REs. Figure 3b shows that there is a linear change in all the CFPs across the lanthanide series apart from the $B_0^2$ and $B_4^4$ parameters at Ce. The change in CFPs caused by the varying nuclear charge of the REs across the lanthanide series should be greatest early in the series because the ionic radii exhibit their greatest relative decrease. It is therefore not unexpected to find a discontinuity in CFPs at Ce. From Eu to Yb, the $B_0^2$ parameter displays a linear decrease down to around zero at Yb. The $B_0^2$ parameter represents the degree of axial asymmetry

experienced by the RE.[38] This indicates that the arrangement of Si atoms around the RE is "stretching" in one axis and the amount of stretching decreases as the ionic radii of the REs decrease across the lanthanide series, as may be expected. The $B_0^4$ and $B_4^4$ parameters are dominated by the covalency of the RE to Si bonds,[39] both these parameters generally decrease linearly across the lanthanide series.

**Table 1.** Goodness of fit ($\sigma$) of various symmetries for the REs. $\sigma = \sqrt{\sum(\Delta_i)^2/(L_{obs} - p)}, \Delta_i = E_{exp} - E_{fit}, L_{obs}$ is the number of lines, $p$ is the number of CFPs, $E_{exp}$ are the experimentally determined energy levels, and $E_{fit}$ are those determined by fitting sets of CFPs.

| Symmetry (CFPs) | Trigonal $(B_0^2 B_0^4 B_3^4 B_0^6 B_3^6 B_6^6)$ | Tetragonal $(B_0^2 B_0^4 B_4^4 B_0^6 B_4^6)$ | Hexagonal $(B_0^2 B_0^4 B_0^6 B_6^6)$ | Cubic $(B_0^4 B_0^6)$ |
|---|---|---|---|---|
| RE | | | | |
| Ce | 209 | 24 | 604 | 2216 |
| Eu | 194 | 31 | 73 | 91 |
| Dy | 75 | 12 | 62 | 210 |
| Ho | 1164 | 52 | 124 | 96 |
| Tm | 61 | 13 | 97 | 106 |
| Yb | 31 | 9 | 27 | 37 |

**Table 2.** Fitted crystal field parameters $(B_0^2 B_0^4 B_4^4 B_0^6 B_4^6)$ representing tetragonal symmetry for various REs-implanted Si and the spin–orbit coupling parameter ($\zeta$), taken from ref.[56] apart from Ce and Eu where $\zeta$ was fitted along with CFPs. Units are $cm^{-1}$.

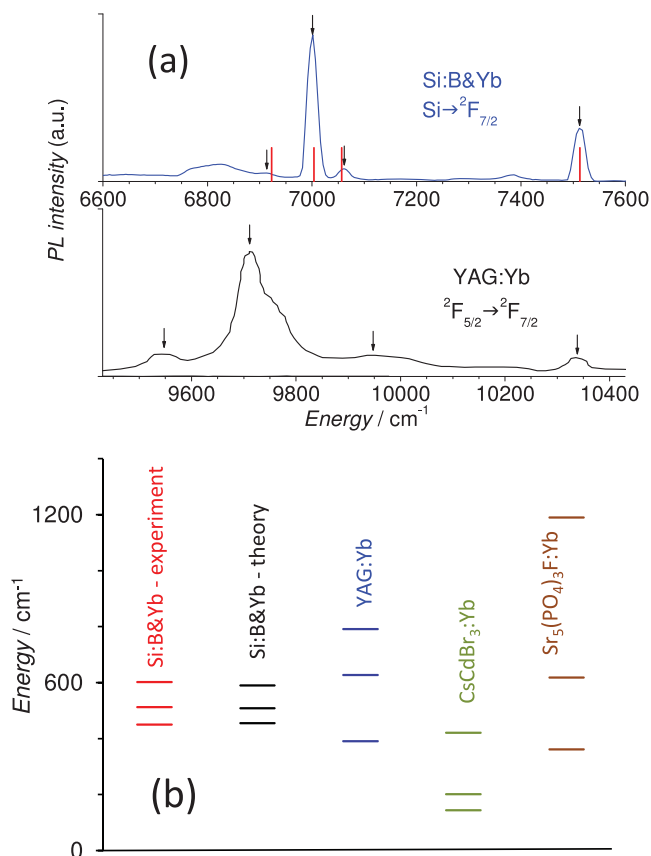| RE | $B_0^2$ | $B_0^4$ | $B_4^4$ | $B_0^6$ | $B_4^6$ | $\zeta$ |
|---|---|---|---|---|---|---|
| Ce | 929 | 310 | −17 | −18 | −20 | 580 |
| Eu | 1095 | −182 | 2034 | 296 | 644 | 1358 |
| Dy | 386 | −555 | 1510 | 201 | 863 | 1913 |
| Ho | 200 | −668 | 1216 | 180 | 949 | 2145 |
| Tm | 100 | −796 | 1098 | 201 | 1077 | 2636 |
| Yb | −3 | −885 | 938 | 193 | 1326 | 2936 |

FULL PAPER



**Figure 4.** Comparison of Yb emission in Si:B&Yb with an Yb emission in YAG:Yb. a) PL spectra of a Si:B&Yb (20 K) and of a YAG:Yb[40] (20 K) as a function of energy. The energy scales for both plots are the same but have been displaced to aid direct comparison of the relative peak positions. Spectra have been matched to the lowest terminal state. The vertical red lines on the Si:B&Yb plot are the theoretical fits obtained from the crystal field analysis; the vertical black arrows indicate the peaks selected for the crystal field analysis. The vertical arrows in the YAG:Yb plot indicate the peak centers in the YAG:Yb spectrum. b) Comparison of experimental splittings from our Si:B&Yb p–n junction data and the theoretical fit obtained from the crystal field analysis. The energy splittings for the $Yb^{3+}$ in three other hosts (YAG,[40] $CsCdBr_3$,[41] and $Sr_5(PO_4)_3F$[41] are also shown.

In Figure 4a, we plot as a function of energy the PL spectrum of the 20 K Si:B&Yb sample and a 20 K PL spectrum from Yb-doped YAG (yttrium aluminium garnet).[40] The experimental and calculated energy splittings for the $Yb^{3+}$ in the Si:B&Yb are shown in Figure 4b. Again, a highly compelling correspondence of the spectral features and the theoretical fit is observed. Figure 4b also shows the $Yb^{3+}$ energy splittings in three other hosts (YAG,[40] $CsCdBr_3$,[41] and $Sr_5(PO_4)_3F$.[41] The wide spread in the $Yb^{3+}$ splittings in different hosts is not atypical and is due to the particular sensitivity of the $Yb^{3+}$ to the crystal field interaction.[41] For example, the $^2F_{7/2}$ manifold overall splitting in $CsCdBr_3$ is only 421 cm$^{-1}$ but is very large (1190 cm$^{-1}$) in $Sr_5(PO_4)_3F$.

Figure 5a,b shows PL spectra of Si:B&Ce sample in the 6500–7350 cm$^{-1}$ range and in the 4600–5350 cm$^{-1}$ range, respectively. Additional weaker sidebands of the main peaks
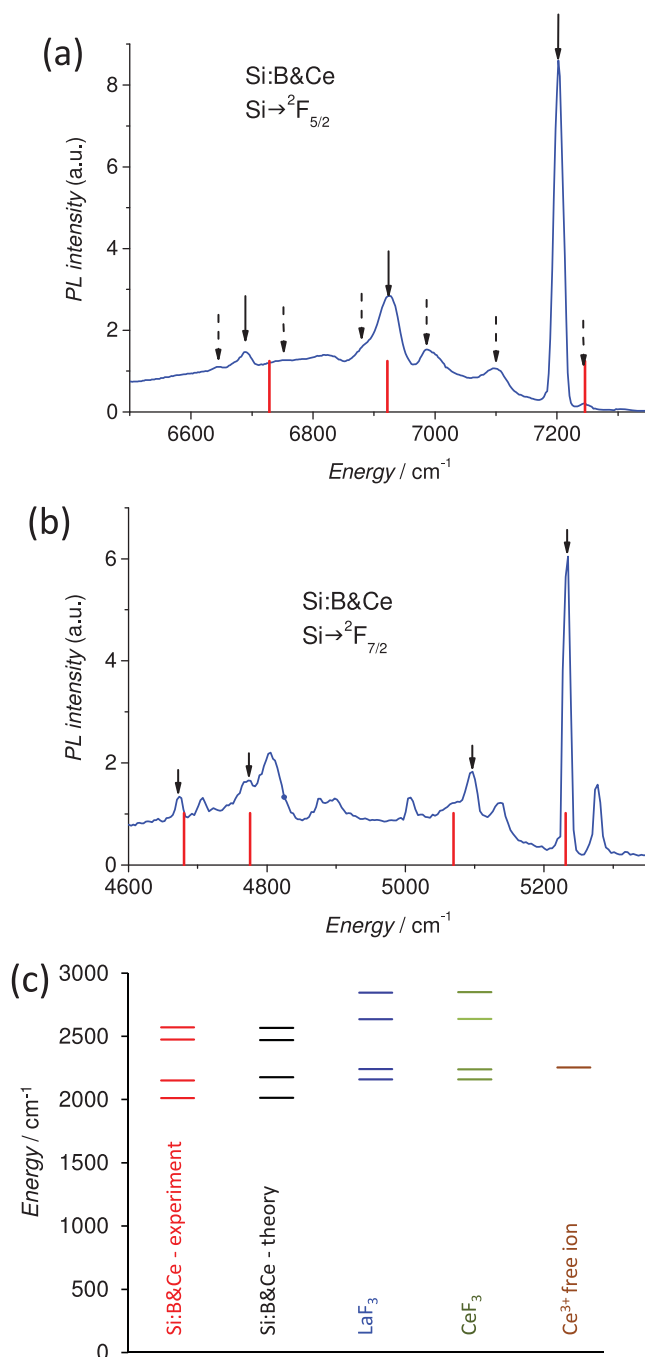


**Figure 5.** Spectra of Ce emission in Si:B&Ce and a comparison with mid-IR absorbance spectra from Ce in other hosts showing the Ce *f–f* transitions. a) Si:B&Ce higher energy range PL spectrum. b) Si:B&Ce lower energy range PL spectrum expanded by a factor of ten. In (a) and (b), the fits for Si:B&Ce are shown as vertical red lines; the solid black arrows indicate the peaks selected for analysis. The dotted arrows indicate additional weaker sidebands of the main peaks attributed to local vibronic modes. c) Comparison of experimental splittings from the lowest $^2F_{5/2}$ ground state to the $^2F_{7/2}$ manifold obtained from the data shown in (a) and (b) with the fit obtained from the crystal field analysis, and with $Ce^{3+}$ transitions from the lowest $^2F_{5/2}$ level to the $^2F_{7/2}$ manifold in $LaF_3$ and in $CeF_3$ measured by mid-IR absorbance.[42] The energy splittings in the free $Ce^{3+}$[43] are also shown.

Materials
Views
www.MaterialsViews.com

ADVANCED
FUNCTIONAL
MATERIALS
www.afm-journal.de

FULL PAPER

are attributed to local vibronic modes. We note that due to the elimination of the unshielded $5d^1$ starting state, this is the first PL associated with Ce in any material that reveals the inherent crystal field splitting of the $^2F_{5/2}$ and $^2F_{7/2}$ manifolds previously only observed in mid-IR absorption.[42] Figure 5c shows a comparison of Si:B&Ce experimental and theoretical splittings from the lowest $^2F_{5/2}$ ground state level to the $^2F_{7/2}$ manifold calculated using the data shown in Figure 5a,b with $Ce^{3+}$ transitions from the lowest $^2F_{5/2}$ level to the $^2F_{7/2}$ manifold in $LaF_3$ and in $CeF_3$ measured by mid-IR absorbance[43] and with the $f$–$f$ splitting of the $Ce^{3+}$ free ion.[43] Again, a strong correspondence of the spectral features in Si:B&Ce and in other hosts is observed.

We conclude that for Eu, Yb, and Ce the silicon band edge has in effect substituted the respective usual starting excited states. Previous observations in the literature, also involving Eu, show significant redshifts of the emission to the 3+ terminal states can occur. In refs.[44] and [45] in the hosts europium gallium garnet doped with chromium and boron nitride codoped with Eu and Cr, Eu–Cr pair emission is observed corresponding to a redshift of the $^5D_0$–$^7F_J$ $Eu^{3+}$ transitions by an amount equal to the energy difference in the $Eu^{3+}$ and $Cr^{3+}$ excited states, showing that the $Cr^{3+}$ ground state has been substituted by the $Eu^{3+}$ ground state. This is attributed to a direct exchange interaction between the ions. Further, in ref.[46] the authors studied a magnetic semiconductor, $Pb_{1-x}Eu_xTe$, a solid solution where Eu is an element of the alloy rather than a dopant as in our case. They observe in addition to the main interband transitions additional lines attributed to transitions from the hybridized conduction band to discrete Stark split $Eu^{3+}$ levels.

The REs can exist in solid hosts in the divalent 2+,[47] trivalent 3+,[47] and more rarely in the tetravalent 4+ state[48] or indeed in more than one valence state in the same host.[49] The highly structured spectra and the fits to the splittings clearly indicate the involvement of the 3+ valence state on a silicon substitutional site as the final terminal state for the optical transitions. Possible excitation mechanisms could be direct charge transfer of an excited electron thermalized at the silicon conduction band edge to the 3+ state followed by a subsequent valence switch of the RE to the 2+ state followed by relaxation back to the 3+ state by electron emission to the valence band. Alternatively we are simultaneously capturing an electron–hole pair or silicon exciton, in both of these cases maintaining the 3+ state.

In the isolated RE ions it is known that the lower 3+ RE levels are far from the vacuum level which has led to a presumption that in narrow band gap semiconductors with low electron affinities these levels would lie deep in the valence band.[50–53] There is however no clear theoretical or experimental data confirming this, in particular in silicon. This presumption is effectively implying that the vacuum levels remain aligned even though the vacuum level has no meaning in the bulk. This concern about the different alignment from the surface or an interface and the bulk has been raised previously for extrapolation of the relative RE energy levels and silicon valence/conduction bands in photoemission experiments.[54] The alignment experimentally observed here suggests that when the REs are incorporated within the bulk of the silicon host, the energy difference is in effect taken up by offsetting the "vacuum level," analogous to that seen in the well-established semiconductor heterojunction systems. **Figure 6** shows the energy levels of $Eu^{3+}$, $Yb^{3+}$, and $Ce^{3+}$ and the proposed effective alignment with the silicon energy band.

An expected consequence of transitions from or fed by a continuum of band states to a RE level, rather than just a single starting state, would be a significant enhancement in the emission intensity. The Eu EL reported here shows an enhancement by a factor of 25 over our best previous "classical" RE device (doped with Tm[27]) and an enhancement of 900 times over our previous best "classical" RE devices in the 1.3–1.5 µm range (doped with either Tm[23] or Er[20]).
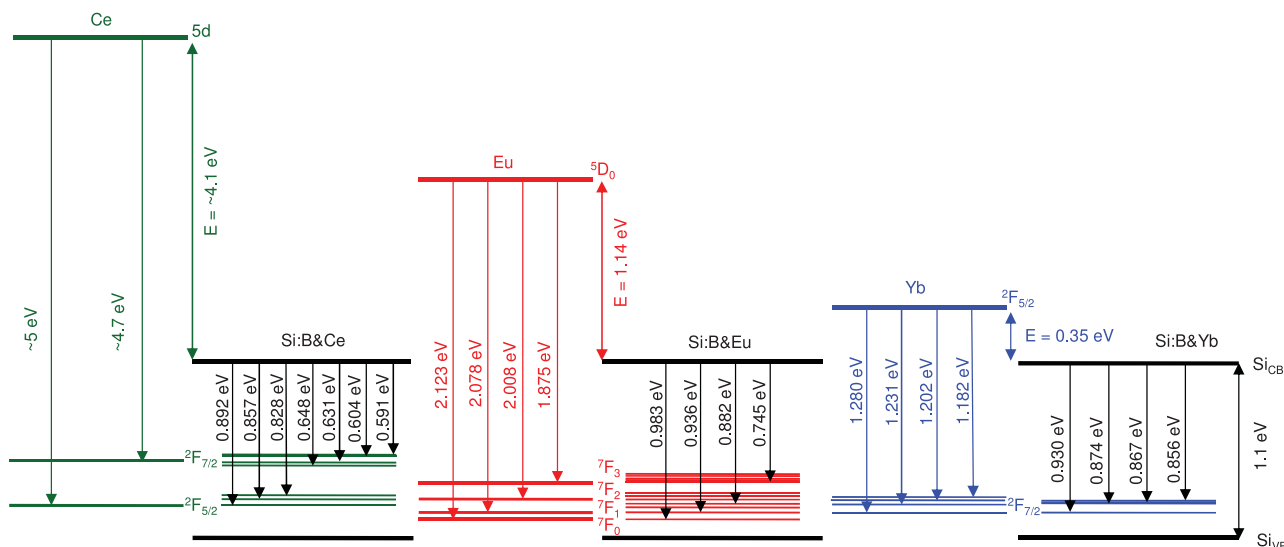


**Figure 6.** Ce, Eu, and Yb energy levels and proposed effective alignment in silicon. Proposed alignment of the internal $Ce^{3+}$, $Eu^{3+}$, and $Yb^{3+}$ manifolds with the silicon energy band. The observed transitions from the silicon conduction band to the $^2F_{7/2}$ and $^2F_{5/2}$ manifolds in $Ce^{3+}$, to the $^7F_J$ levels in $Eu^{3+}$, and to the $^2F_{7/2}$ ground state manifold in $Yb^{3+}$ are indicated. For comparison, the characteristic lowest energy internal transitions from GdOBr:$Ce^{3+}$ (excited with 245 nm from Xe-continuous wave (Xe-CW) source[33], ZnO:$Eu^{3+}$[30] and YAG:$Yb^{3+}$[40]) are also indicated.
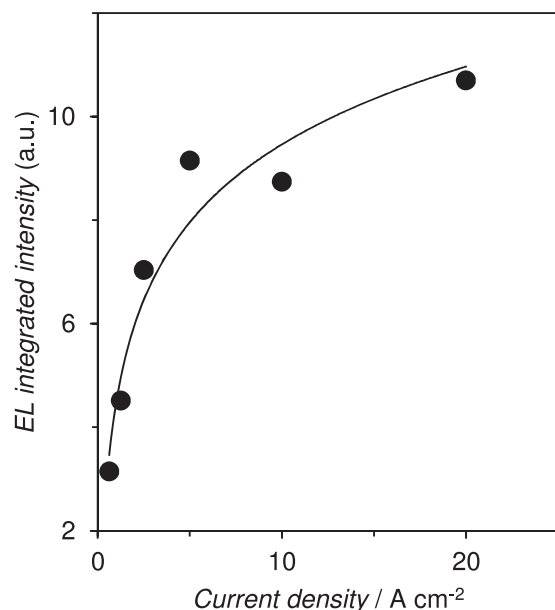
**Figure 7.** Light output against operating current density for the Si:B&Eu diode. The measurements were performed at 80 K.

The light output against operating current density for the Si:B&Eu diode is shown in **Figure 7**. The sublinear behavior at the higher current densities is the result of sample heating that quenches the EL. We have calculated the internal quantum efficiency ($QE_{int}$) using the method described in detail in the Experimental Section. We obtain a value in the linear regime, at a current density of 2 A cm$^{-2}$, of 8% for the $QE_{int}$. The $QE_{int}$ is the product of the radiative efficiency and the carrier injection efficiency implying a lower limit for the most critical parameter, the radiative efficiency of 8%, assuming 100% injection efficiency. In practice the injection efficiency, which we have not so far attempted to optimize, is likely to be much lower than unity and so the radiative efficiency will be correspondingly higher.

## 2.2. Silicon Mid-IR Photodetectors (SMIRPs)

Intrinsic RE transitions are internal to the RE and do not contribute directly to carrier conduction in the bands of the host. Consequently, this makes them of limited use as a basis for optical detectors. The band-edge-modified RE levels exampled here interact directly with the silicon bands and so offer the possibility of extrinsic photovoltaic or photoconductive detectors. The wavelengths that could be detected using Eu, Yb, and Ce cover wavelengths from the near-IR at 1.1 µm, the band gap of silicon, out to the mid-IR for the lowest energy valence band to RE transitions. We have observed photoresponse from our diodes. An example of our Si:B&Eu diode being used as a SMIRP is shown in **Figure 8**, where we plot the specific detectivity $D^*$ from 1 to 6 µm (the current limit of our measurement system). For comparison, we also plot the detectivity of a control silicon diode without the Eu doping but otherwise identically processed and of existing state-of-the-art commercially available detectors.[55] Our recent SMIRPs, designed as photodiodes by placing the Eu in the depletion region, have shown much
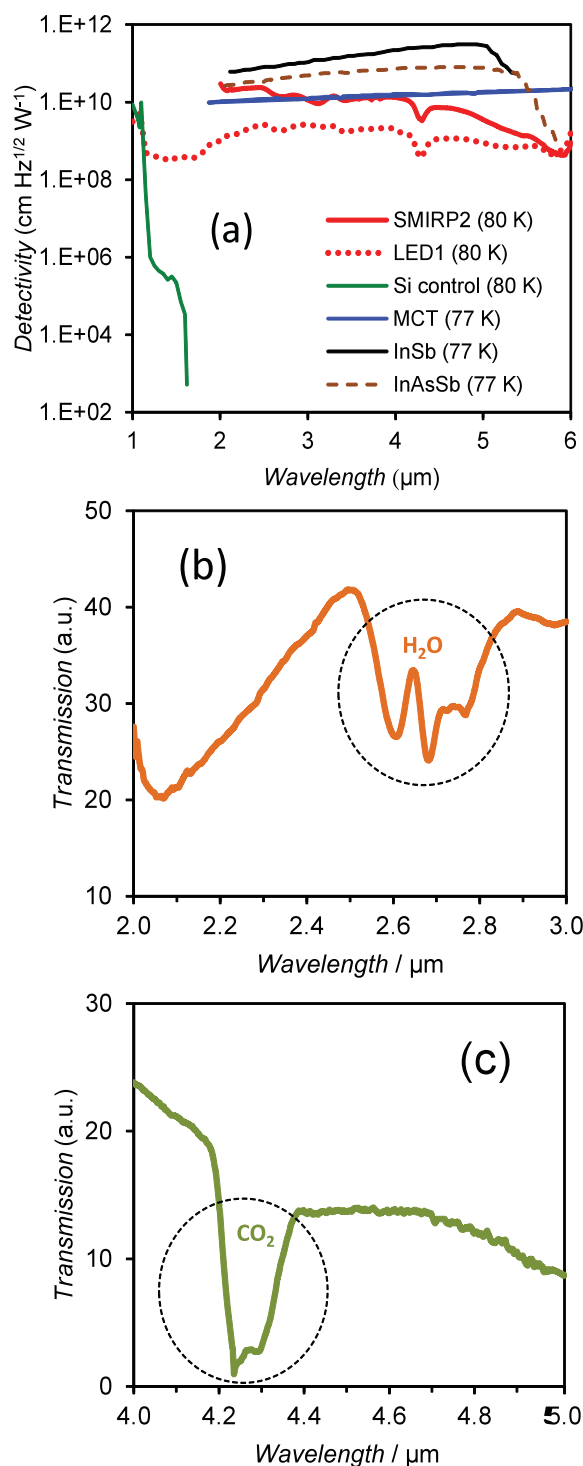


**Figure 8.** Detector characteristics for Eu doped silicon diodes. a) Specific detectivity $D^*$ from 1 to 6 µm of the Si:B&Eu diode shown in Figure 1 used as detector (LED1), of a control silicon diode without the Eu doping but otherwise identically processed and of existing state-of-the-art commercially available detectors (MCT, InSb, and InAsSb[55]). Also shown is the detectivity of a recent device (SMIRP2) designed as a photodiode by placing the Eu in the depletion region. Parts (b) and (c) show transmission spectra measured with our first device (LED1) showing the water vapor and $CO_2$ absorption lines present at ambient levels, respectively. The optical path length through the air was 1 m.

![Materials Views logo]
www.MaterialsViews.com

ADVANCED
FUNCTIONAL
MATERIALS
www.afm-journal.de

FULL PAPER

improved detectivities as seen in Figure 8. It can be seen that our latest detectors at 4 μm already have specific detectivity as good as state-of-the-art mercury cadmium telluride (MCT) detectors and are close to the best available detectors in this spectral region. In Figure 8b,c, we show transmission spectra measured with our original detector showing the important water vapor and $CO_2$ absorption lines present at ambient levels in the air.

## 3. Conclusion

In summary, we report the first and surprising observation of redshifted Eu, Yb, and Ce emission in silicon and demonstrate IR LEDs operating under conventional forward bias. All emissions are massively redshifted in wavelength from those expected. This has been attributed to the direct intercession of the silicon providing a primary state replacing the usual intrinsic excited $Eu^{3+}$, $Yb^{3+}$, and $Ce^{3+}$ states, $^5D_0$, $^7F_{5/2}$, and the $5d^1$ levels, respectively. The direct involvement of the bulk band state continua rather than a single excited starting state and the absence of the usually required "third party" energy transfer mechanisms are highly significant as both changes leads to much greater effective optical emission, as evidenced here by up to a 900-fold enhancement of EL intensity at the key 1.3–1.5 μm optical communication wavelength compared to classical RE devices. These observations suggest that current presumptions of the alignment of RE levels when incorporated in the bulk of semiconductors should be revisited.

In addition we have demonstrated the first silicon mid-IR photodetector with specific detectivities—the key figure of merit—comparable to current state-of-the-art mid-IR detectors. We note that strained silicon and SiGe alloys, both of which vary the band gap energy, are now used in state-of-the-art CMOS (complementary metal oxide semiconductor) technology and could be used to provide additional tuning of the modified RE transitions.

The exemplars, Si:B&Eu, Si:B&Yb, and Si:B&Ce, demonstrated here, by themselves, offer access to emitters and detectors across a wide range of wavelengths opening up new discrete and integrated photonics technologies scanning much of the near- and mid-IR.

## 4. Experimental Section

*Crystal Field Analysis*: Crystal field analysis was carried out using both our method described in ref.[14] and the program SPECTRA developed at Argonne National Laboratory and available at http://chmwls.chm.anl.gov/downloads/index.html. SPECTRA had an advantage over our previous methodology in that it is able to fit multiple *f*-shell manifolds simultaneously and it uses a differential evolution algorithm to determine a global minimum which gave a significant reduction in computation time. Our method and SPECTRA gave very similar results. For the Si:B&Yb only the four PL lines expected from the $^2F_{7/2}$ manifold were observed and five lines are needed to obtain the five CFPs. Therefore the lower level of the $^2F_{5/2}$ manifold in Yb:YAG from ref. [41] was used to enable a valid fit and confirm the Yb tetragonal symmetry. The largely host independent free ion parameters were taken from fitted absorption spectra of REs in $LaF_3$.[56] However, for Si:B&Ce and Si:B&Eu, we found that fitting the spin–orbit coupling parameter (ζ) gave a more satisfactory fit but did not vary significantly from previously published values.[56,57] ζ is given in Table 2.

*Device Fabrication*: Si:B&RE (RE = Ce, Eu, Ho, and Yb) structures were fabricated by B implantation ($10^{15}$ B $cm^{-2}$ at 30 keV) into n-type Si [100] substrates. Some substrates were annealed after B implantation at 950 °C for times ranging from 30 s to 20 min. Subsequently 400 keV RE ions were implanted ($10^{13}$–$10^{14}$ ions $cm^{-2}$ range) and annealed either at 800 or 850 °C for times up to 5 min. The optimum processing conditions to achieve the brightest RE luminescence in silicon is similar for most of the REs and has been discussed in detail in ref.[27]. The implant energy chosen placed the REs on the p-side of the junction outside the depletion region. A second generation of Si:B&Eu devices were specifically engineered as photodetectors, which required Eu implantation at multiple energies chosen to ensure that the Eu was uniformly distributed across the depletion region at zero bias. The depletion width at zero bias is ≈2 μm. The diffusion length of the REs for the maximum anneal temperature and time used here (850 °C/5 min) is ≈0.02 μm,[58] which is much less than the depletion width.

*Device Characterization*: EL and PL were measured between 20 K and room temperature from 1000 to 2200 nm using an InGaAs detector. The EL was performed under forward bias and the light was extracted through a window in the back electrode.[20] Current–voltage measurements were made and diode characteristics were observed with typical turn-on voltages of ≈0.5 V. For the PL experiments, the samples were excited by a 532 nm diode pumped laser line at a power density of ≈3 kW $m^{-2}$.

Quantum efficiency measurements were made by first obtaining the external power efficiency, optical power out over electrical power in, by absolute measurements of the electrical power (drive current × operating voltage) in to the LED and optical power out. The optical power out was measured with a calibrated large area broad band power meter placed after the collecting optics. The power meter was an Ophir Laser Star fitted with a PD300 IR head. The total optical power out of the device can then be calculated taking in to account the efficiency of the collecting optics. The external power efficiency can then be calculated. The external quantum efficiency is then given by the power efficiency times the drive voltage divided by the energy per photon. The internal quantum efficiency can then be calculated by multiplying the external quantum efficiency by the device optical extraction efficiency which is the product of the absorption, Fresnel and internal reflection losses. The Fresnel and internal reflection losses can be obtained directly from the known refractive indices of silicon, and air. As the emission is well below the silicon band gap the absorption losses are taken to be zero.

The initial photodetection measurements were made at 80 K on the same LEDs but in unbiased photovoltaic mode. The diodes were illuminated through the window in the back of the sample and the photovoltage was measured using a lock-in amplifier. The specific detectivity D* (cm $Hz^{1/2}$ $W^{-1}$) was calculated using the usual formula for an unbiased detector in photovoltaic mode,[59] $D* = R_i \times (R_0A/4kT)^{1/2}$, where $R_i$ is the responsivity (A $W^{-1}$), A is the area of detector ($cm^2$), k is Boltzmann's constant, T is the absolute temperature (K), and $R_0$ is the dynamic resistance (Ω). The spectral responsivity measurements between 1.2 and 6 μm were obtained by illuminating the detector through a SPEX 1680 (0.22 m) double monochromator fitted with 4 μm gratings and order sorting filters (1.05, 1.65, 2.4, and 3.6 μm). The IR source was a Newport 6363 IR emitter operated at 90 W with a color temperature of 1050 K. Power measurements as a function of wavelength were made using a calibrated Newport optical power meter 1916-C. The dynamic resistance was obtained from current–voltage measurements at 80 K using an Agilent B1505 parameter analyzer. This methodology was validated by applying it over the same spectral range to a calibrated Hamamatsu MCT detector (Type P9697-02) of known spectral responsivity, dynamic impedance, specific detectivity, and detector size.

**FULL PAPER**

[1] W. L. Ng, M. A. Lourenço, R. M. Gwilliam, S. Ledain, G. Shao, K. P. Homewood, *Nature* **2001**, *410*, 192.

[2] A. S. Liu, R. Jones, L. Liao, D. Samara-Rubio, D. Rubin, O. Cohen, R. Nicolaescu, M. Paniccia, *Nature* **2004**, *427*, 615.

[3] O. Boyraz, B. Jalali, *Opt. Express* **2004**, *12*, 5269.

[4] V. R. Almeida, C. A. Barrios, R. R. Panepucci, M. Lipson, *Nature* **2004**, *431*, 1081.

[5] H. S. Rong, R. Jones, A. S. Liu, O. Cohen, D. Hak, A. Fang, M. Paniccia, *Nature* **2005**, *433*, 725.

[6] S. G. Cloutier, P. A. Kossyrev, J. Xu, *Nat. Mater.* **2005**, *4*, 887.

[7] R. S. Jacobsen, K. N. Andersen, P. I. Borel, J. Fage-Pedersen, L. H. Frandsen, O. Hansen, M. Kristensen, A. V. Lavrinenko, G. Moulin, H. Ou, C. Peucheret, B. Zsigri, A. Bjarklev, *Nature* **2006**, *441*, 1922.

[8] A. W. Fang, H. Park, O. Cohen, R. Jones, M. J. Paniccia, J. E. Bowers, *Opt. Express* **2006**, *14*, 9203.

[9] M. A. Foster, A. C. Turner, J. E. Sharping, B. S. Schmidt, M. Lipson, A. L. Gaeta, *Nature* **2006**, *441*, 960.

[10] D. D. Berhanuddin, M. A. Lourenço, R. M. Gwilliam, K. P. Homewood, *Adv. Funct. Mater.* **2012**, *22*, 2709.

[11] S. Wirths, R. Geiger, N. von den Driesch, G. Mussler, T. Stoica, S. Mantl, Z. Ikonic, M. Luysberg, S. Chiussi, J. M. Hartmann, H. Sigg, J. Faist, D. Buca, D. Gruetzmacher, *Nat. Photonics* **2015**, *9*, 88.

[12] J. J. Ackert, D. J. Thomson, L. Shen, A. C. Peacock, P. E. Jessop, G. T. Reed, G. Z. Mashanovich, A. P. Knights, *Nat. Photonics* **2015**, *9*, 393.

[13] R. Soref, *Nat. Photonics* **2010**, *4*, 495.

[14] M. A. Hughes, M. A. Lourenço, D. J. Carey, B. Murdin, K. P. Homewood, *Opt. Express* **2014**, *22*, 29292.

[15] H. Ennen, J. Schneider, G. Pomrenke, A. Axmann, *Appl. Phys. Lett.* **1983**, *43*, 943.

[16] B. Zheng, J. Michel, F. Y. G. Ren, L. C. Kimerling, D. C. Jacobson, J. M. Poate, *Appl. Phys. Lett.* **1994**, *64*, 2842.

[17] G. Franzò, F. Priolo, S. Coffa, A. Polman, A. Carnera, *Appl. Phys. Lett.* **1994**, *64*, 2235.

[18] A. Polman, *J. Appl. Phys.* **1997**, *82*, 1.

[19] A. J. Kenyon, *Semicond. Sci. Technol.* **2005**, *20*, R65.

[20] M. A. Lourenço, M. Milosavljević, S. Galata, M. S. A. Siddiqui, G. Shao, R. M. Gwilliam, K. P. Homewood, *Vacuum* **2005**, *78*, 551.

[21] M. A. Lourenço, R. M. Gwilliam, K. P. Homewood, *Appl. Phys. Letts.* **2007**, *91*, 141122.

[22] G. S. Pomrenke, E. Silkowski, J. E. Colon, D. J. Topp, Y. K. Yeo, R. L. Hengehold, *J. Appl. Phys.* **1992**, *71*, 1919.

[23] M. A. Lourenço, R. M. Gwilliam, K. P. Homewood, *Appl. Phys. Lett.* **2008**, *92*, 161108.

[24] M. A. Lourenço, R. M. Gwilliam, K. P. Homewood, *Opt. Lett.* **2011**, *36*, 169.

[25] A. J. Kenyon, *Prog. Quantum Electron.* **2002**, *26*, 225.

[26] M. A. Lourenço, Z. Mustafa, W. Ludurczak, L. Wong, R. M. Gwilliam, K. P. Homewood, *Opt. Lett.* **2013**, *38*, 3669.

[27] M. A. Lourenço, W. Ludurczak, A. D. Prins, M. Milosavljević, R. M. Gwilliam, K. P. Homewood, *Jpn. J. Appl. Phys.* **2015**, *54*, 07JB01.

[28] J. Sawahata, H. Bang, J. Seo, K. Akimoto, *Sci. Technol. Adv. Mater.* **2005**, *6*, 644.

[29] T. Andreev, N. Q. Liem, Y. Hori, M. Tanaka, O. Oda, D. L. S. Dang, B. Daudin, *Phys. Rev. B* **2006**, *73*, 195203.

[30] Y. Liu, W. Luo, R. Li, G. Liu, M. R. Antonio, X. Chen, *J. Phys. Chem. C* **2008**, *112*, 686.

[31] T. Koubaa, M. Dammak, M. Kammoun, W. M. Jadwisienczak, H. J. Lozykowski, A. Anders, *J. Appl. Phys.* **2009**, *106*, 013106.

[32] C. E. Mungan, M. I. Buchwald, B. C. Edwards, R. I. Epstein, T. R. Gosnell, *Mater. Sci. Forum* **1997**, *239–241*, 501.

[33] C. H. Kam, S. Buddhudu, *Mater. Lett.* **2002**, *54*, 337.

[34] G. Davies, *Phys. Rep.* **1989**, *176*, 83.

[35] R. Sauer, J. Weber, J. Stolz, E. R. Weber, K. H. Kusters, H. Alexander, *Appl. Phys. A* **1985**, *36*, 1.

[36] B. G. Wybourne, L. Smentek, *Optical Spectroscopy of Lanthanides: Magnetic and Hyperfine Interactions*, Taylor & Francis, Boca Raton, FL **2007**.

[37] K. R. Lea, M. J. M. Leask, W. P. Wolf, *J. Phys. Chem. Solids* **1962**, *23*, 1381.

[38] P. Pal, T. Penhouet, V. D'Anna, H. Hagemann, *J. Lumin.* **2013**, *134*, 678.

[39] D. J. Newman, B. Ng, *Crystal Field Handbook*, Cambridge University Press, Cambridge **2007**.

[40] J. Dong, K. Ueda, H. Yagi, A. A. Kaminskii, in *Advances in Solid State Lasers Development and Applications* (Ed. M. Grishin), InTech, Rijeka, Croatia **2010**.

[41] P.-H. Haumesser, R. Gaume, B. Viana, E. Antic-Fidancev, D. Vivien, *J. Phys.: Condens. Matter* **2001**, *13*, 5427.

[42] I. Szczygiel, L. Macalik, E. Radominska, T. Znamierowska, M. Maczka, P. Godlewska, J. Hanuza, *Opt. Mater.* **2007**, *29*, 1192.

[43] R. A. Buchanan, H. E. Rast, H. H. Caspers, *J. Chem. Phys.* **1966**, *44*, 4063.

[44] J. P. Van Der Ziel, L. G. Van Uitert, *Phys. Rev.* **1969**, *186*, 332.

[45] E. M. Shishonok, S. V. Leonchik, J. W. Steeds, *Phys. Status Solidi B* **2007**, *244*, 2172.

[46] I. I. Zasavitskii, A. V. Mazurin, Y. G. Selivanov, H. Zogg, A. V. Yurushkin, *JETP Lett.* **2008**, *87*, 498.

[47] G. H. Dieke, *Spectra and Energy Levels of Rare Earth Ions in Crystal*, John Wiley & Sons, New York, NY **1968**.

[48] D. R. Mullins, S. H. Overbury, D. R. Huntley, *Surf. Sci.* **1998**, *409*, 307.

[49] E. Kaldis, A. Schlegel, P. Wachter, Ch. Zurcher, *J. Magn. Magn. Mater.* **1976**, *3*, 1.

[50] S. Schmitt-Rink, C. M. Varma, A. F. J. Levi, *Phys. Rev. Lett.* **1991**, *66*, 2782.

[51] M. Needels, M. Schluter, M. Lannoo, *Phys. Rev. B* **1993**, *47*, 15533.

[52] I. N. Yassievich, L. C. Kimerling, *Semicond. Sci. Technol.* **1993**, *8*, 718.

[53] T. Schweizer, P. E.-A. Mobert, J. R. Hector, D. W. Hewak, W. S. Brocklesby, D. N. Payne, G. Huber, *Phys. Rev. Lett.* **1998**, *80*, 1537.

[54] T. Tiedje, K. M. Colbow, Y. Gao, J. R. Dahn, J. N. Reimers, D. C. Houghton, *Appl. Phys. Lett.* **1992**, *61*, 1296.

[55] Characteristics and use of infrared detectors, https://hamamatsu.com/resources/pdf/ssd/infrared_kird9001e/pdf, **2011**, acessed January 2016.

[56] W. T. Carnall, G. L. Goodman, K. Rajnak, R. S. Rana, *J. Chem. Phys.* **1989**, *90*, 3443.

[57] C.-K. Duan, P. A. Tanner, *J. Phys. Chem. A* **2010**, *114*, 6055.

[58] D. É. Nazyrov, *Semiconductors* **2003**, *37*, 551.

[59] J. L. Johnson, L. A. Samoska, A. C. Gossard, J. L. Merz, M. D. Jack, G. R. Chapman, B. A. Baumgratz, K. Kosai, S. M. Johnson, *J. Appl. Phys.* **1996**, *80*, 1116.